Atmospheric
Chemistry
and Physics

Supplement of

Atmospheric gaseous hydrochloric and hydrobromic acid in urban Beijing, China: detection, source identification and potential atmospheric impacts

Xiaolong Fan et al.

Correspondence to: Lei Yao (lei.yao@helsinki.fi) and Yee Jun Tham (thamyj@mail.sysu.edu.cn)

Section S1. ACSM, MARGA, Aethalometer and NO-NO$_2$-NO$_X$ Analyzer

Table S1. Instruments

	Phase	
	Gas	Particulate
CI-APi-LTOF	√	×
ACSM	×	√
MARGA	√	√
Aethalometer (AE33)	×	√
NO-NO$_2$-NO$_X$ Analyzer	√	×

ACSM

An online Time-of-Flight-Aerosol Chemical Speciation Monitor (ToF-ACSM, Aerodyne Research Inc., US, hereafter ACSM) was deployed to measure nitrate, sulphate, ammonium, chloride and organic at the same site with a PM$_{2.5}$ aerodynamic lens and standard vaporizer. Particles first went through a PM$_{2.5}$ cyclone and then a 3-m steel tube before being analyzed by ToF-ACSM. The ionization efficiency (IE) and relative ionization efficiency (RIE) of Cl were obtained by calibrations with pure standards of ammonium nitrate and ammonium chloride. It should be noted that the Cl measured by ACSM was non-refractory chloride compounds such as ammonium chloride. Yet, a high correlation was observed between Cl measured by aerosol mass spectrometry and automated ion chromatography method such as particle into liquid sampler (PILS), which measured total water-soluble Cl in previous studies (Canagaratna et al., 2007). It suggested that the non-refractory Cl measured by ACSM could explain large proportion of particulate Cl in the urban environment. In addition, the contribution of crustal materials was relatively low during the winter season (He et al., 2001; Yu et al., 2013), further supporting that its contribution to refractory Cl should be minor during our sampling period.

MARGA

The Monitor for AeRosols and Gases (MARGA, Metrohm AG Inc., Switzerland) is an online analyzer that semi-continuously measures water-soluble gases (i.e., HCl, HONO, HNO$_3$, SO$_2$, NH$_3$) and chemical composition of aerosols (i.e., Cl$^-$, NO$_3^-$, SO$_4^{2-}$, Na$^+$, NH$_4^+$, K$^+$, Mg^{2+}, Ca^{2+}) at an hourly temporal resolution using ion chromatography. The ambient sample containing gaseous species and PM$_{2.5}$ particles passes through a wet rotating denuder (WRD). WRD has two concentric glass cylinders coated with absorption solution (H$_2$O$_2$), which causes the gas to diffuse into aqueous film (Keuken et al., 1988; Otjes et al., 1993; Rumsey et al., 2011). The samples are analyzed by using cation and anion ion conductivity detectors (IC, Metrohm AG Inc., Switzerland). The analytical accuracy was controlled by internal standard LiBr, which is injected simultaneously and then mixed with the sample. In addition, to verify the accuracy of HCl concentration, an external standard test was conducted by replacing the absorption solution with a known liquid anion standard containing Cl$^-$ (sigma-aldrich, multielement ion chromatography anion standard solution, containing F$^-$, Cl$^-$, NO$_3^-$, PO$_4^{3-}$, SO$_4^{2-}$) every week.

Aethalometer (AE33) and NO-NO$_2$-NO$_X$ Analyzer

Black carbon (BC) mass concentrations were measured by the aethalometer (Model AE33, Magee Scientific Inc., USA). Particles first went through a PM$_{2.5}$ cyclone and the aerosol sample were collected continuously on the filter tape. Two measurements are obtained from the loaded and unloaded spot, which from same air stream, with different rates of accumulation of the aerosol sample. The transmission of light was measured at 7 different wavelengths. AE33 calculates the instantaneous concentration of optically absorbing aerosols from the rate of change of the attenuation of light transmitted through the particle-laden filter (Drinovec et al., 2014) and then provides the compensated particle light absorption

and BC concentration. In this study, aerosol particles are continually sampled on filter and the optical attenuation is measured with high time resolution.

The NO_2 concentrations were measured with a THERMO 42i NO-NO_2-NO_X Analyzer (Thermal Environment Instruments Inc. USA).
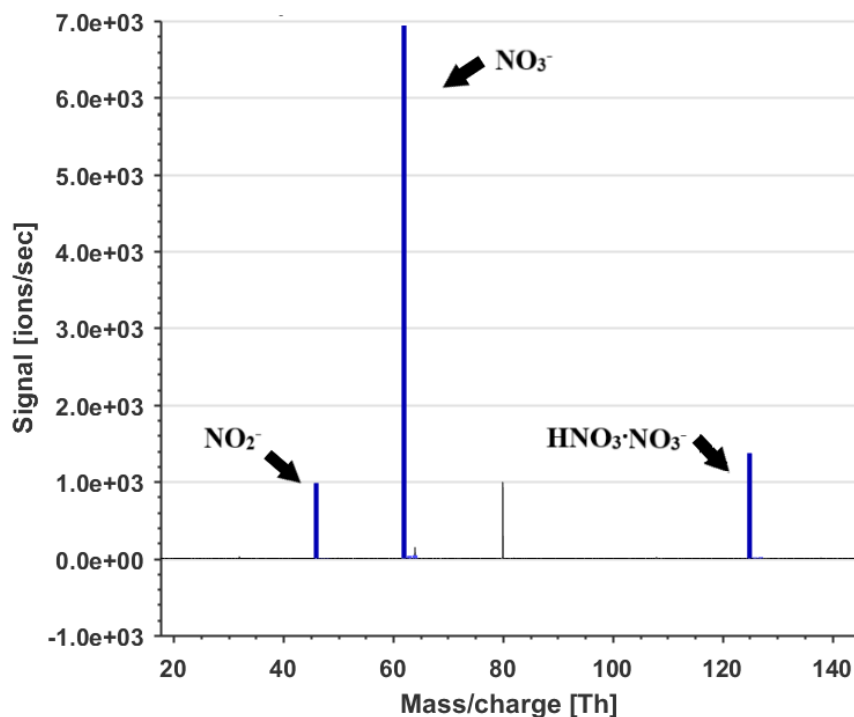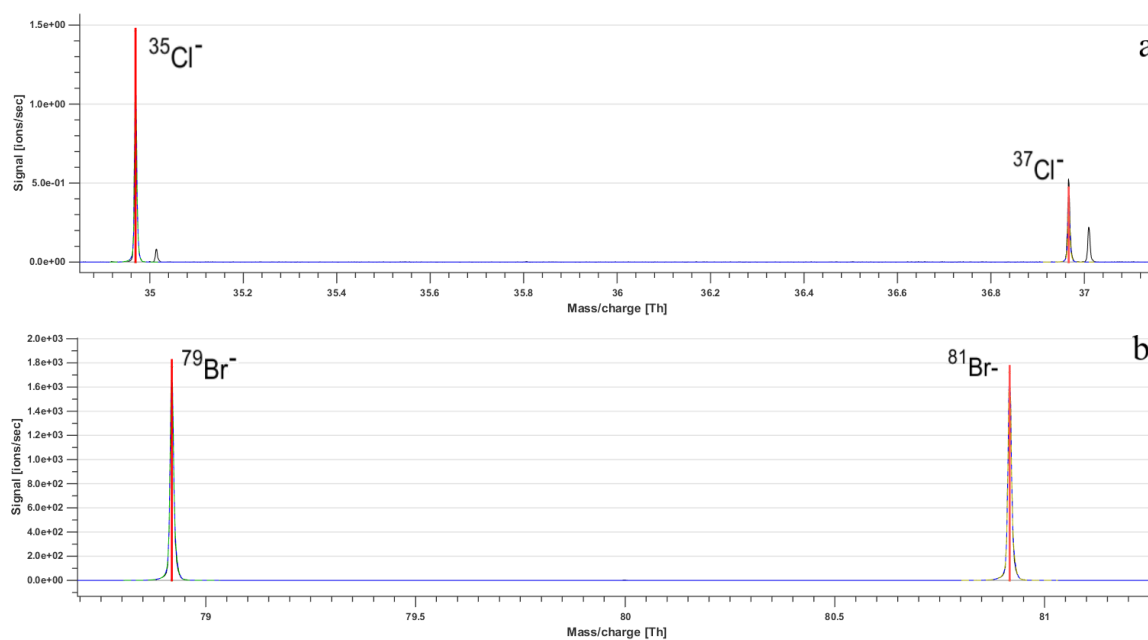
90

95

100

105

110

115

120

125

130

Section S2. A typical raw mass spectrum and high-resolution peak fittings of interested compounds
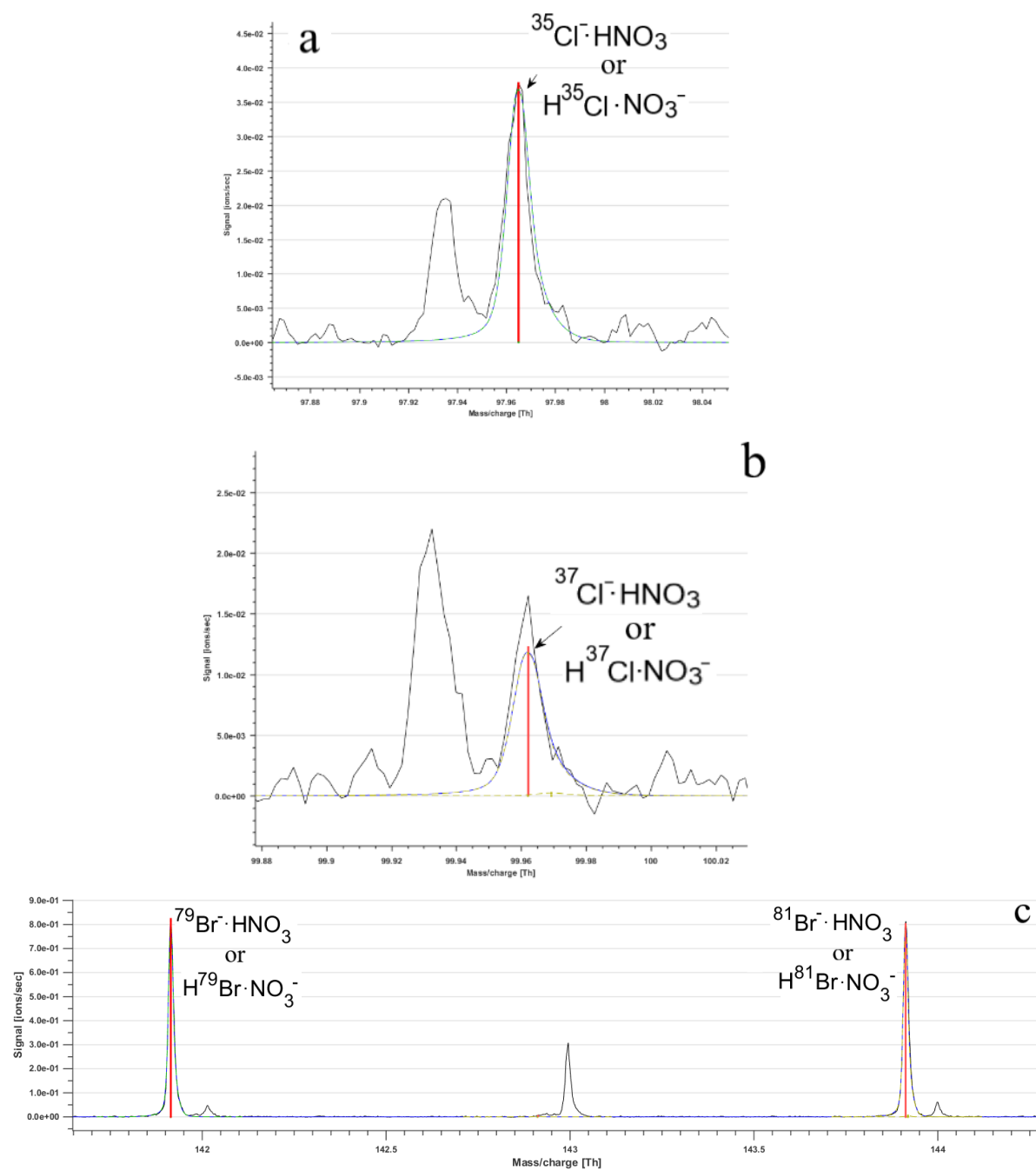

Figure S1. Reagent ion signals of NO_2^-, NO_3^- and $HNO_3 \cdot NO_3^-$.

Figure S2. High resolution peak fitting of $^{35}Cl^-$ and $^{37}Cl^-$, which has the same ratio ($^{35}Cl^-:^{37}Cl^- = 3:1$) as isotopic abundances of the chlorine elements (**a**); High resolution peak fitting of ^{79}Br and $^{81}Br^-$, which has the same ratio ($^{79}Br^-:^{81}Br^- = 1:1$) as isotopic abundances of the bromine elements (**b**).

Figure S3. High resolution peak fitting of $^{35}Cl·HNO_3$ (or $H^{35}Cl·NO_3^-$) (**a**), $^{37}Cl·HNO_3$ (or $H^{37}Cl·NO_3^-$) (**b**), $^{79}Br·HNO_3$ (or $H^{79}Br·NO_3^-$) and $^{81}Br·HNO_3$ (or $H^{81}Br·NO_3^-$) (**c**).

Section S3. Cluster stabilities

Initial geometries of molecules were generated by performing a molecular mechanics (MMFF) conformer sampling using the Spartan 18' program (Benson et al., 2008). All molecules and clusters studied here had only one possible conformer geometry. The molecules were optimized using density functional methods at the ωB97X-D/aug-cc-pVTZ level (ωB97X-D/aug-cc-pVTZ-PP for bromide containing molecules) and ultrafine integration grid with the Gaussian 16 program (Yu et al., 2017). Bromide pseudopotential definitions were taken from EMSL basis set library (Wang et al., 2017; Wilson et al., 1999). Single-point calculations on the optimized geometries were carried out at the DLPNO-CCSD(T)/def2-QZVPP level using the ORCA program version 4.0.0.2 (Neese, 2012; Riplinger and Neese, 2013) to provide the accurate final energies used to calculate the cluster binding enthalpies. The predicted sensitivities were derived by inputting the calculated binding enthalpies into the model presented in Iyer et al. (2016).
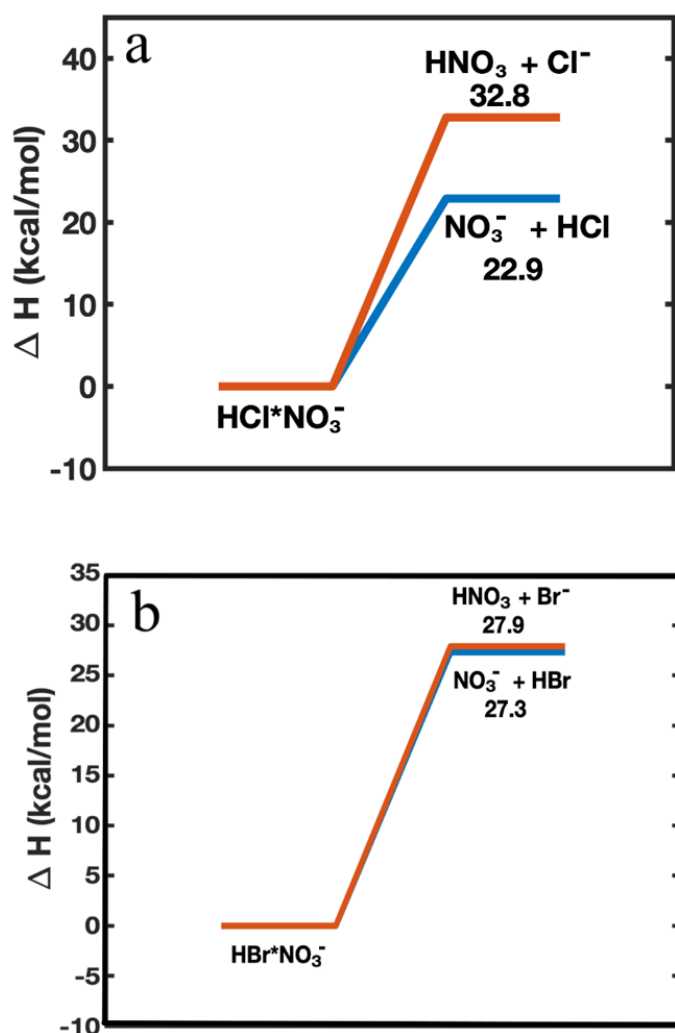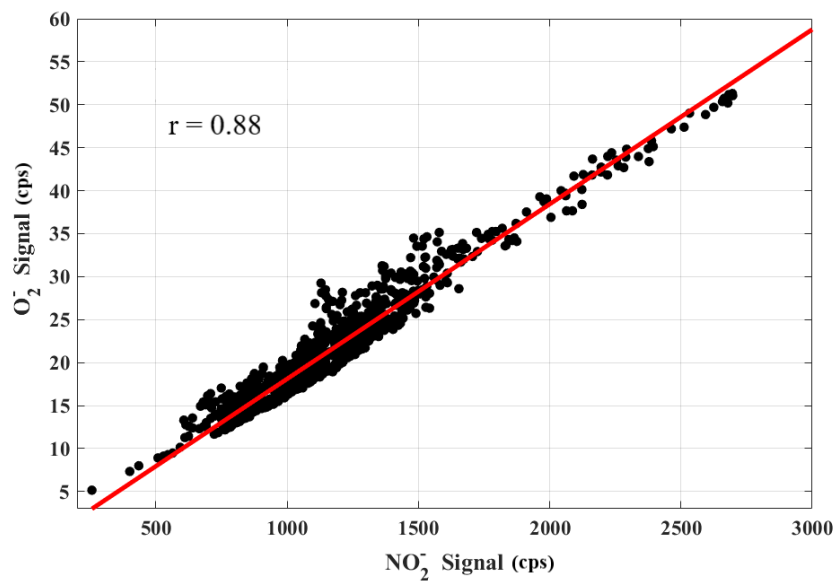

Figure S4. (a) The enthalpies of HCl·NO$_3^-$ formed by HNO$_3$ + Cl$^-$ and NO$_3^-$ + HCl and **(b)** the enthalpies of HBr·NO$_3^-$ formed by HNO$_3$ + Br$^-$ and NO$_3^-$ + HBr calculated at the DLPNO-CCSD(T)/def2-QZVPP// ωB97X-D/aug-cc-pVTZ-PP level of theory.

Figure S5. High correlation (r = 0.88) between NO_2^- and O_2^- ion signals (with 1095 valid data points) during observation periods.

Section S4. Laboratory experiment of detection of HCl and HBr

In order to quantitively confirm HCl and HBr can be detected by CI-APi-LTOF, 1 ml liquid standard HCl (Gaosheng, 36%) and HBr (Macklin, 48%) were diluted in 1000 ml MILLIPORE® ultrapure water resulting in 1.2×10^{-2} mol L^{-1} HCl and 8.6×10^{-3} mol L^{-1} HBr, respectively. Then, 10 ml diluted HCl and HBr solution was put in a U-shape glass tube and then the mixed flow of evaporated HCl and HBr and zero air (1L min^{-1}) went into CI-APi-LTOF (Figure S6). After the injection of gaseous HCl and HBr, the signals of Cl^-, Br^-, $Cl^-\cdot HNO_3$ (or $HCl\cdot NO_3^-$) and $Br^-\cdot HNO_3$ (or $HCl\cdot NO_3^-$) started to increase (Figure S7), confirming that the HCl and HBr can be detected as Cl^-, Br^-, $Cl^-\cdot HNO_3$ (or $HCl\cdot NO_3^-$) and $Br^-\cdot HNO_3$ (or $HBr\cdot NO_3^-$) by CI-APi-LTOF.

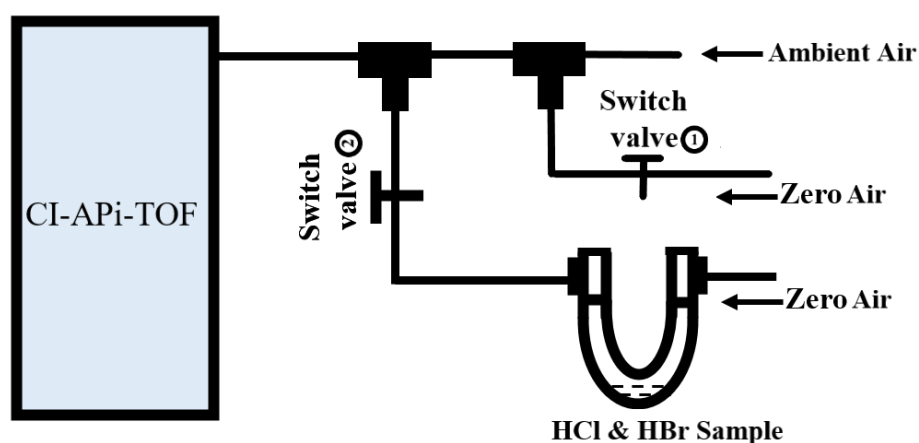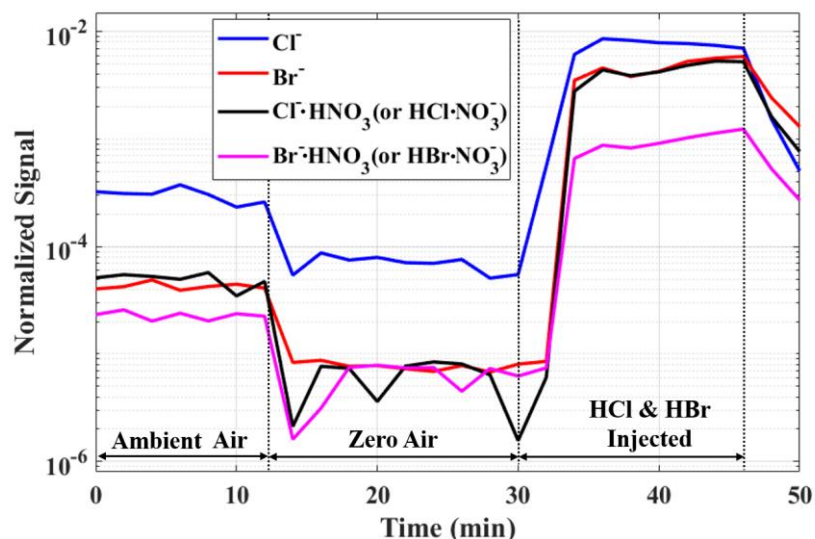**Figure S6.** Schematic of the laboratory experiment set up.

Figure S7. Time profile of normalized Cl^-, Br^-, $Cl^-\cdot HNO_3$ (or $HCl\cdot NO_3^-$) and $Br^-\cdot HNO_3$ (or $HBr\cdot NO_3^-$) signals measured by CI-APi-LTOF during the laboratory test. Within the duration from 0 to 12min, ambient air was sampled and measured by CI-APi-LTOF. The signals of zero air generated from a pure air generator (AADCO 737) were treated as background signals. The detection limits of HCl and HBr were obtained as three times the standard deviation of background signals within a 2 min integration time. After the injection of gaseous HCl and HBr which evaporated from HCl and HBr solution, the elevated Cl^-, Br^-, $Cl^-\cdot HNO_3$ (or $HCl\cdot NO_3^-$) and $Br^-\cdot HNO_3$ (or $HBr\cdot NO_3^-$) signals were observed.

Section S5. Calibration factor and Uncertainty estimation

The HCl and HBr were measured by a NO_2^--based chemical ionization long time-of-flight mass spectrometer (CI-APi-LTOF). Direct calibrations for HCl and HBr were not available. In order to calibrate HCl concentration, we adopt the ambient gaseous HCl concentrations measured by MARGA for about 4 days (02.09.2019 to 06.09.2019) to indirectly calibrate the CI-APi-LTOF. Time profile of HCl concentration from MARGA and normalized signals of HCl by sum of NO_2^- and O_2^- ion from CI-APi-LTOF was depicted in Figure S8. From Figure S8a, it shows similar variation of the data from two different instruments. Figure S8b showed HCl concentration measured by MARGA versus HCl normalized signal measured by CI-APi-LTOF. Data from MARGA correlates well with HCl normalized signal ($r = 0.73$).

A time-of-flight aerosol chemical speciation monitor (ToF-ACSM, Aerodyne Research Inc., USA) equipped with a $PM_{2.5}$ aerodynamic lens was applied to measure the particulate non-refractory Cl. The detailed introduction for ToF-ACSM with $PM_{2.5}$ lens and its comparison with other instruments could be found in previous literature (Xu et al., 2017;Zheng et al., 2020;Zhang et al., 2017). Although ACSM only measures the non-refractory Cl, a high correlation was achieved for the comparison between ACSM and MARGA measurement ($r=0.98$, intercept=0.067, shown in Figure S8d), suggesting non-refractory Cl measured by ACSM could explain a large proportion of particulate Cl in our sampling period.
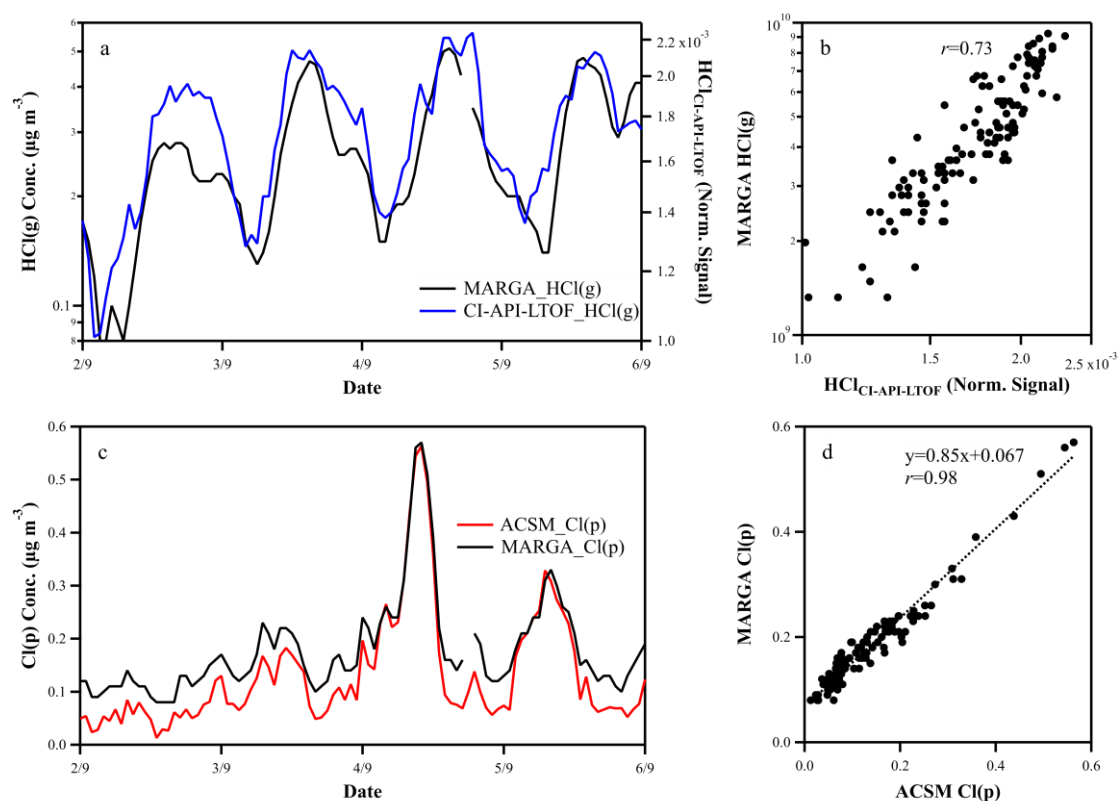
Figure S8. Time series of normalized HCl signals measured by CI-APi-LTOF and HCl(g) measured by MARGA during the calibration period (i.e., 2 to 6 September 2019) (**a**); The correlation between HCl(g) concentrations and normalized HCl signals measured by CI-APi-LTOF (**b**); Time series of particulate Cl (Cl(p)) measured by MARGA and ACSM (**c**); The correlation between particulate Cl (Cl(p)) measured by MARGA and ACSM (**d**).

Table S2. Estimated uncertainty factors in HCl quantification.

	Relative uncertainty (δ)
MARGA measurement	0.15
Intercomparison between MARGA and CI-APi-TOF	0.24

260　　　　The uncertainties of HCl and HBr measurement come from two parts:

(1) the HCl measurement uncertainties coming from MARGA (δ_{MARGA}) and (2) fitting errors coming from the intercomparison between MARGA and CI-APi-LTOF measurements ($\delta_{MARGA-LTOF}$). The total uncertainties were calculated with the uncertainties propagation equation shown in Eq. (S1). The δ_{MARGA} was obtained from many previous studies and assumed to be 15% (Trebs et al., 2004; Du et al., 2010, 265　　2011; Wang et al., 2013). The $\delta_{MARGA-LTOF}$ was calculated through a procedure implemented in MATLAB (Mathworks, Inc.) from the fitting errors between HCl concentrations measured by MARGA and normalized HCl signals from CI-APi-LTOF in the intercomparison from the period of 2 to 6 September 2019 (shown in Table S2 and Figure S8). $\delta_{MARGA-LTOF}$ was varied from 11% to 24% according to the fitting calculations (with 95% confidence bounds). To be more conservative, $\delta_{MARGA-LTOF}$ of 0.24 was 270　　applied into Eq. (S1) to calculate the total uncertainty (δ). Therefore, the total uncertainty of $\pm$ 30% was estimated in reporting HCl concentrations. The uncertainties for HBr were assumed to be the same with HCl since it is assumed that HCl and HBr have the same sensitivities for CI-APi-LTOF.

$$\delta = \sqrt{\delta_{MARGA}^2 + \delta_{MARGA-LTOF}^2} = \sqrt{(0.15)^2 + (0.24)^2} = 0.28 \qquad \text{Eq. (S1)}$$

275

　　　　It should be noted that our assumptions of uncertainties could be regarded as a lower limit of HCl and HBr measurement since other potential uncertainty factors (e.g., different sensitivities of HCl and HBr) were not taken into account.

280

285

290

295

Section S6. PSCF Analysis

The Potential Source Contribution Function model (MeteoInfo PSCF modelling) were used to evaluate the transport pathways and potential source affecting HCl and HBr concentration in this study. Only the high concentrations of HBr and HCl (>75th percentile, mainly around the middle of the day due to the diurnal patterns) were linked to the trajectories and presented. The 24-h trajectories analysis were conducted by HYSPLIT GDAS data with the ending height of 100 m. The higher potentials of transport pathways led to high concentration indicates the possible source regions. Details of PSCF could be found in Wang et al., (2014&2019). The time-series of HBr concentration during the whole sampling period and those applied in the PSCF analysis were exhibited in Figure S9b. It is shown that only the extremely high HBr concentrations were included in the trajectory and PSCF analysis, coincidence with the period of heavy pollution indicated by the high $PM_{2.5}$ concentration level (>80 µg m^{-3} and ~100 µg m^{-3} for HBr and HCl, respectively). Meanwhile, the lower HBr concentrations during the nighttime and clean periods were not included in the PSCF analysis.

Additionally, Cl/Br-containing particles would have a longer lifetime in the atmosphere from hours to weeks for fine particles in the troposphere (Seinfeld, 2003) and continuously influence the gaseous HBr concentration through gas-particle partitioning. Therefore, in this study, the 24h-backwards air mass trajectory and PSCF analyses were adopted to indicate the source regions of the polluted air masses that result in the high Cl and Br levels rather than the real-time origins of gaseous HCl/HBr in the atmosphere. A shorter time in trajectory analysis, on the other hand, would increase the uncertainties in calculations and may not provide more information on source regions of air parcels at a large scale.
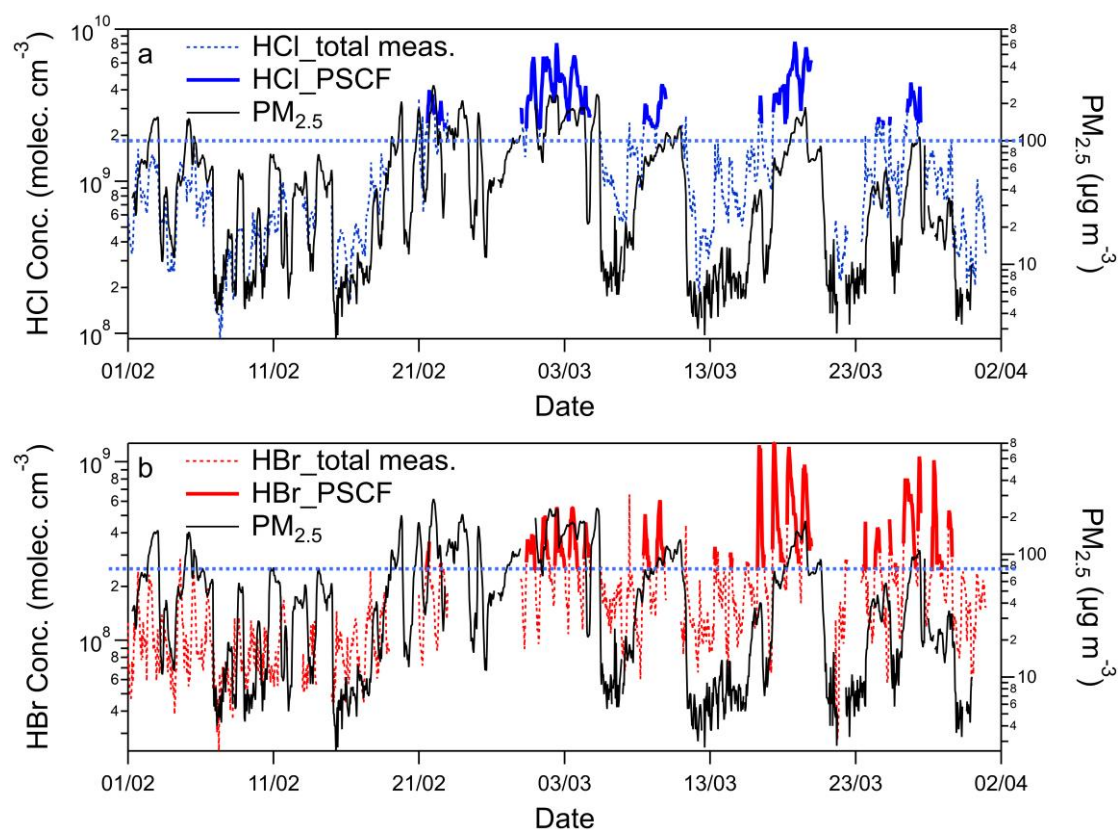
Figure S9. Time series of gaseous HCl during the whole sampling period, those in PSCF analysis (>75th percentile) and $PM_{2.5}$ mass concentrations (**a**), and gaseous HBr during the whole sampling period, those in PSCF analysis (>75th percentile) and $PM_{2.5}$ mass concentrations (**b**).
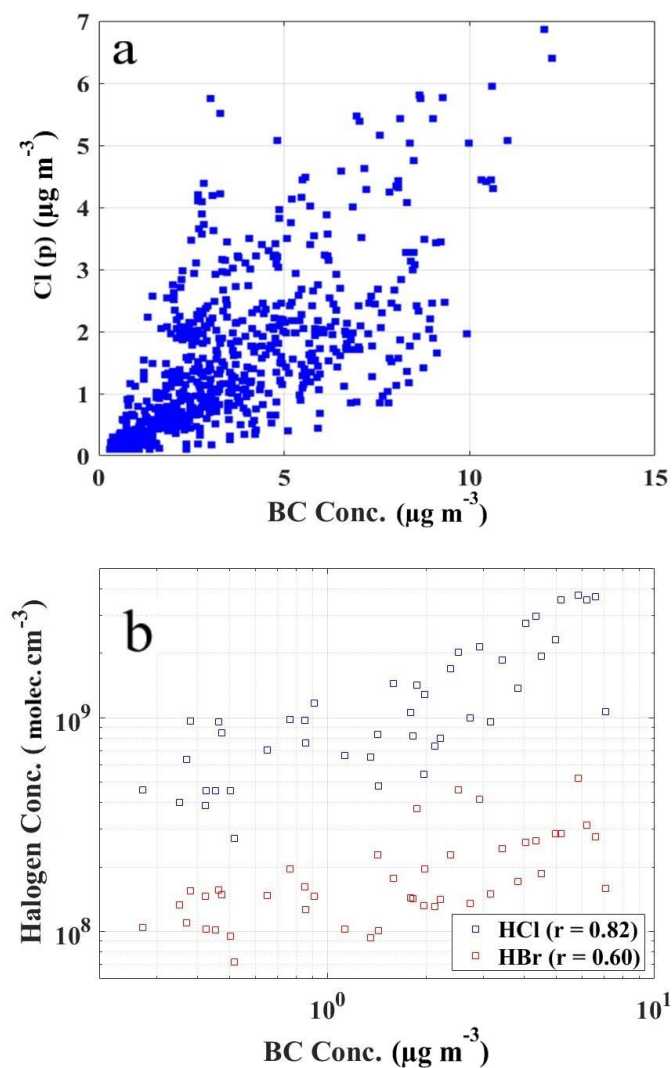
Section S7. Source identification

Figure S10. The correlation ($r = 0.67$) between hourly mean mass concentrations of particulate Cl (Cl(p)) and black carbon (BC) (**a**); correlations between daily mean concentrations of HCl ($r = 0.82$), HBr ($r = 0.60$) and BC during observation periods from 1 February to 31 March, 2019 (**b**).

Section S8. The calculations of OH concentration and production rates of atomic Cl and Br.

OH concentration:

In this work, there is no direct measurement of OH radical concentration during observation periods. While during the winter and spring in Beijing, it has been found that the measured OH radical concentration is linearly correlated with photolysis rate of ozone, J_{OID} (Liu et al., 2020; Tan et al., 2019). Thus, an empirical equation was proposed to estimate the OH concentrations: $[OH] = J_{OID} \times 2 \times 10^{11}$ molecules cm^{-3}. We adopted this empirical equation to calculate the OH concentration in this study.

We further validated our calculation by comparing the OH concentration, obtained with another method suggested by Xu et al. (2015), which considering both photolysis rate (J_{OID} and J_{NO_2}) and NO$_2$ concentration C_{NO_2} based on formula equation (S2). Using another dataset collected from 21 May to 10 June 2019 where the parameters of J_{NO_2} and C_{NO_2} were available from direct measurements, a good correlation ($r = 0.97$) was achieved between measured J_{NO_2} and predicted J_{NO_2}, which was derived from the solar zenith angle and the location using a box model (FACSIMILE 4) (Liu et al., 2020), confirming the validation of our predicted J_{NO_2} (Figure S11a).

$$C_{OH} = \frac{4.1 \times 10^9 \times (J_{O1D})^{0.83} \times (J_{NO_2})^{0.19} \times (140 C_{NO_2} + 1)}{0.41 C_{NO_2}^2 + 1.7 C_{NO_2} + 1} \qquad \text{Eq. (S2)}$$

Production rates of atomic Cl and Br:

In order to determine the impacts of gas particle partitioning of HCl and HBr on atmospheric oxidation capacity and particulate chloride and bromine, an accurate measurement of gas phase HCl and HBr are required to assess the production rate of Cl and Br atoms via direct OH oxidation of HCl and HBr. The Cl· and Br· can be formed via the reactions (R (S1) and R (S2)) of HCl and HBr with OH.

$$HO + HCl \rightarrow H_2O + Cl^{\cdot} \qquad \text{R(S1)}$$
$$HO + HBr \rightarrow H_2O + Br^{\cdot} \qquad \text{R(S2)}$$
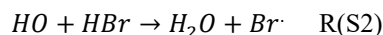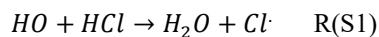
Thus, $Cl^{\cdot}$ and $Br^{\cdot}$ radical production rate P_{Cl} and P_{Br} can be calculated based on formula Eq. (S3) and Eq. (S4), respectively.

$$P_{Cl} = k_{Cl} \times [HCl] \times [OH] \qquad \text{Eq. (S3)}$$
$$P_{Br} = k_{Br} \times [HBr] \times [OH] \qquad \text{Eq. (S4)}$$

where, rate coefficient $k_{Cl} = 1.7 \times 10^{-12} \times \exp(-230/T)$ cm^3 molecule^{-1} s^{-1} over the temperature range 200-300 K and $k_{Br} = 6.7 \times 10^{-12} \times \exp(155/T)$ cm^3 molecule^{-1} s^{-1} over the temperature range 180-370 K were obtained from IUPAC (http://iupac.pole-ether.fr.). [HCl], [HBr] and [OH] stand for HCl, HBr and OH concentrations.
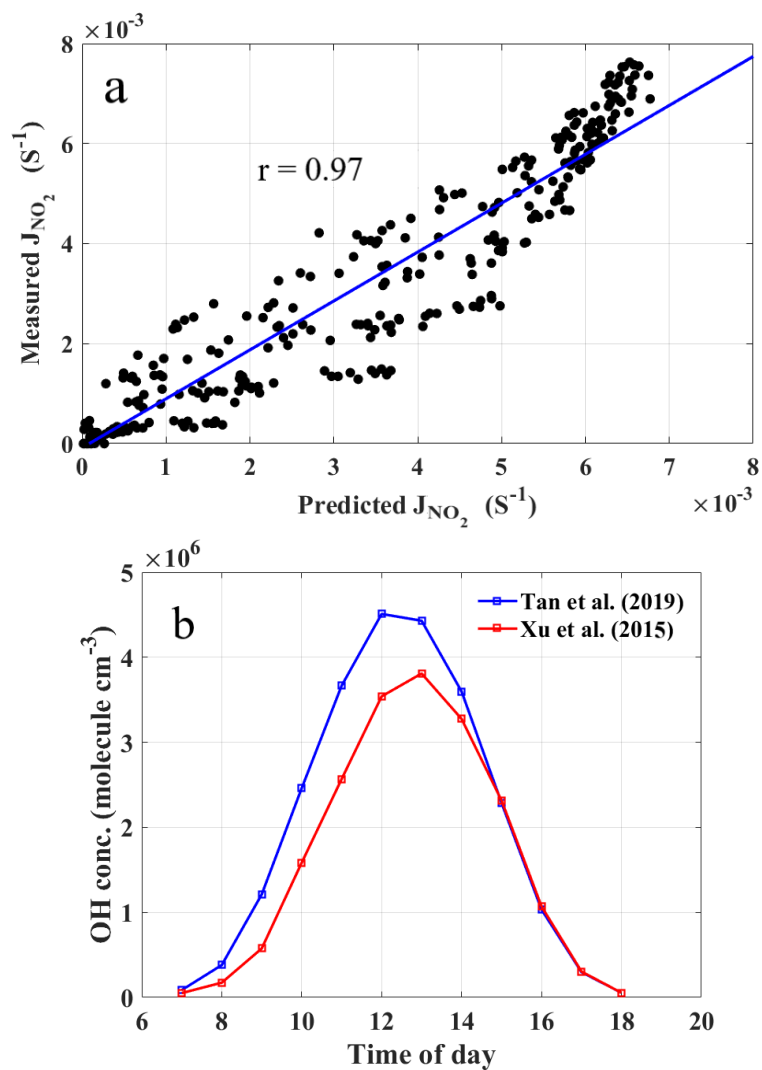
Figure S11. High correlation ($r = 0.97$) between measured and predicted J_{NO_2} from 21 May to 10 June 2019 (**a**); Calculated diurnal curves of OH concentration based on Tan et al., (2019) and Xu et al., (2015) from 1 February to 31 March 2019 (**b**).
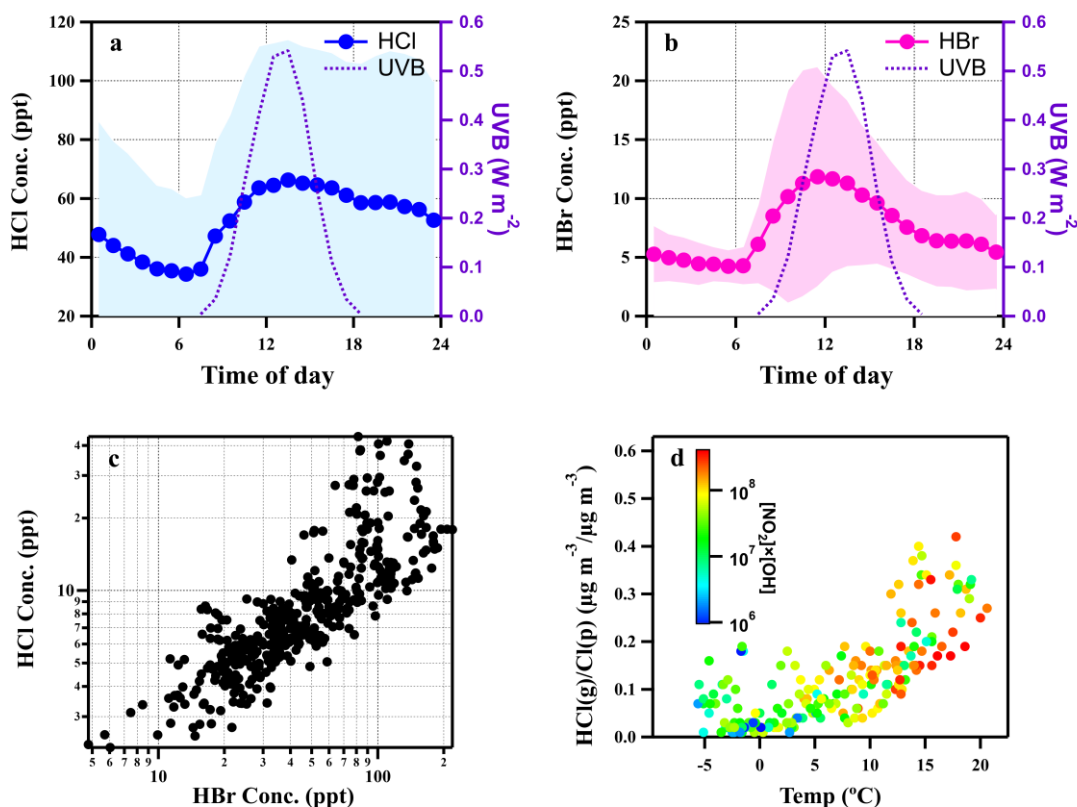
395

400

405

410

415

Figure S12. Diurnal variations of UVB intensities, HCl and HBr concentrations (averaged values ± one standard deviation) (**a** and **b**) and the correlation between HCl and HBr (**c**). Temperature dependence of gas to particle partitioning ratios of mass concentration of chloride, colour-coded by $[NO_2]*[OH]$ which was indicated as the abundance of HNO_3 during daytime (**d**). In panel c and d, the data points are hourly averaged ones during daytime (8:00-17:00).All snowy and rainy days during the sampling period were excluded. Note that the plots are similar to those in Figure 4 of the main text, but this is displayed as pptv.
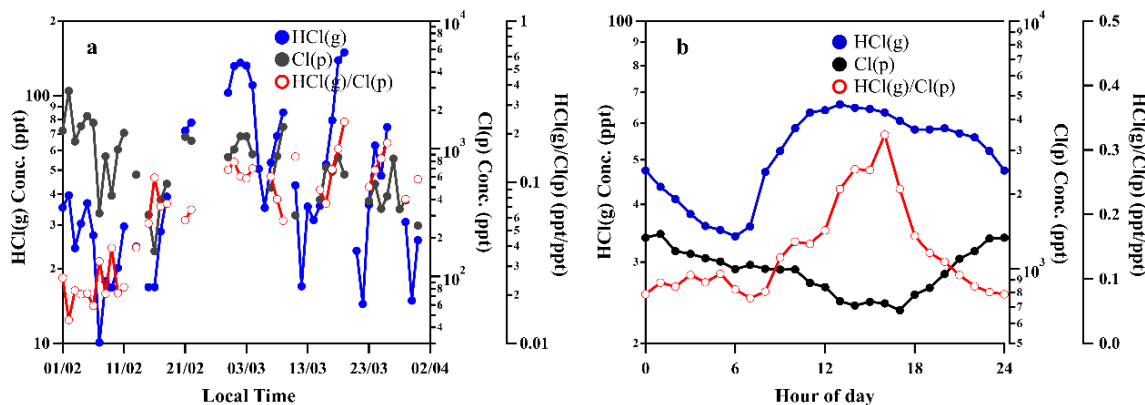
Figure S13. Time variation of daily averaged concentration of particulate chloride (Cl(p)) measured by ACSM, gaseous HCl (HCl(g)) measured by CI-APi-LTOF and mole ratios of HCl(g)/Cl(p) (**a**), and diurnal variation of HCl(g), Cl (p) and mole ratios of HCl(g)/Cl(p) (**b**). Note that the plots are similar to those in Figure 5 of the main text, but this is displayed as pptv.

References：

Benson, D.R., Young, L.H., Lee, S.H., Campos, T.L., Rogers, D.C., Jensen, J., 2008. The effects of airmass history on new particle formation in the free troposphere: case studies. Atmos. Chem. Phys. 8, 3015-3024.

Canagaratna, M.R., Jayne, J.T., Jimenez, J.L., Allan, J.D., Alfarra, M.R., Zhang, Q., Onasch, T.B., Drewnick, F., Coe, H., Middlebrook, A., Delia, A., Williams, L.R., Trimborn, A.M., Northway, M.J., DeCarlo, P.F., Kolb, C.E., Davidovits, P., Worsnop, D.R., 2007. Chemical and microphysical characterization of ambient aerosols with the aerodyne aerosol mass spectrometer. Mass Spectrom Rev 26, 185-222.

Du, H.H., Kong, L.D., Cheng,T.T., Chen, J.M., Yang, X., Zhang, R.Y., Han,Z.W., Yan, Z., Ma, Y.L.: Insights into ammonium particle-to-gas conversion: non-sulfate ammonium coupling with nitrate and chloride. Aerosol Air Qual. Res. 10, 589–595, 2010

Du, H.H., Kong, L.D., Cheng, T.T., Chen, J.M., Du, J.F., Li, L., Xia, X.G., Leng, C.P., Huang, G.H.: Insights into summertime haze pollution events over Shanghai based on online water-soluble ionic composition of aerosols. Atmos. Environ. 45, 5131–5137, 2011

Drinovec, L., Močnik, G., Zotter, P., Prévôt, A.S.H., Ruckstuhl, C., Coz, E., Rupakheti, M., Sciare, J., Müller, T., Wiedensohler, A., 2014. The "dual-spot" Aethalometer: an improved measurement of aerosol black carbon with real-time loading compensation. Atmospheric Measurement Techniques 8, 1965-1979.

He, K.B., Yang, F.M., Ma, Y.L., Zhang, Q., Yao, X.H., Chan, C.K., Cadle, S., Chan, T., Mulawa, P., 2001. The characteristics of $PM_{2.5}$ in Beijing, China. Atmospheric Environment 35, 4959-4970.

Iyer, S., Lopez-Hilfiker, F., Lee, B., Thornton, J., Kurtén, T., 2016. Modeling the Detection of Organic and Inorganic Compounds Using Iodide-Based Chemical Ionization. The journal of physical chemistry. A 120.

Keuken, M.P., Schoonebeek, C.A.M., van Wensveen-Louter, A., Slanina, J., 1988. Simultaneous sampling of NH_3, HNO_3, HC1, SO_2 and H_2O_2 in ambient air by a wet annular denuder system. Atmospheric Environment (1967) 22, 2541-2548.

Liu, Y., Zhang, Y., Lian, C., Yan, C., Feng, Z., Zheng, F., Fan, X., Chen, Y., Wang, W., Chu, B., Wang, Y., Cai, J., Du, W., Daellenbach, K. R., Kangasluoma, J., Bianchi, F., Kujansuu, J., Petäjä, T., Wang, X., Hu, B., Wang, Y., Ge, M., He, H., and Kulmala, M.: The promotion effect of nitrous acid on aerosol formation in wintertime in Beijing: the possible contribution of traffic-related emissions, Atmos. Chem. Phys., 20, 13023-13040, 10.5194/acp-20-13023-2020, 2020.

Neese, F., 2012. The ORCA program system. Wiley Interdisciplinary Reviews: Computational Molecular Science 2, 73-78.

Otjes, R.P., Wyers, G.P., Slanina, J., 1993. A continuous-flow denuder for the measurement of ambient concentrations and surface-exchange fluxes of ammonia. Atmospheric Environment Part A General Topics 27, 2085-2090.

Riplinger, C., Neese, F., 2013. An efficient and near linear scaling pair natural orbital based local coupled cluster method. Journal of Chemical Physics 138, 064103.

Rumsey, I.C., Cowen, K.A., Kelly, T.J., Hanft, E.A., Walker, J.T., 2011. An assessment of the performance of the Monitor for AeRosols and GAses in ambient air (MARGA): A semi-continuous method for soluble compounds. Atmospheric Chemistry and Physics 14, 0327.

Seinfeld, J. H.: TROPOSPHERIC CHEMISTRY AND COMPOSITION | Aerosols/Particles, in: Encyclopedia of Atmospheric Sciences, edited by: Holton, J. R., Academic Press, Oxford, 2349-2354, 2003.

Tan, Z., Lu, K., Jiang, M., Su, R., Zhang, Y., 2019. Daytime atmospheric oxidation capacity in four Chinese megacities during the photochemically polluted season: A case study based on box model simulation. Atmospheric Chemistry and Physics 19, 3493-3513.

Trebs, I., Meixner, F., Slanina, J., Otjes, R., Jongejan, P., and Andreae, M.: Real-time measurements of
480   ammonia, acidic trace gases and water-soluble inorganic aerosol species at a rural site in the Amazon Basin, Atmospheric Chemistry and Physics, 4, 967-987, 10.5194/acp-4-967-2004, 2004.

Wang, L., Du, H., Chen, J.-M., Zhang, M., Huang, X., Tan, H., Kong, L., and Geng, F.: Consecutive transport of anthropogenic air masses and dust storm plume: Two case events at Shanghai, China, Atmospheric Research, 127, 22–33, 10.1016/j.atmosres.2013.02.011, 2013.

485 Wang, Y. Q.: MeteoInfo: GIS software for meteorological data visualization and analysis, Meteorological Applications, 21, 2014.

Wang, Y. Q.: An Open Source Software Suite for Multi-Dimensional Meteorological Data Computation and Visualisation, Journal of Open Research Software, 7, 10.5334/jors.267, 2019.

Wang, Z., Wu, Z., Yue, D., Shang, D., Guo, S., Sun, J., Ding, A., Wang, L., Jiang, J., Guo, H., Gao, J.,
490   Cheung, H.C., Morawska, L., Keywood, M., Hu, M.,: New particle formation in China: Current knowledge and further directions. Sci. Total Environ. 577, 258-266, 2017

Wilson, A.K., Woon, D.E., Peterson, K.A., Dunning, T.H., 1999. Gaussian Basis Sets for Use in Correlated Molecular Calculations. IX. The Atoms Gallium Through Krypton. The Journal of Chemical Physics 110, 7667-7676.

495 Xu, Z., Wang, T., Wu, J., Xue, L., Chan, J., Zha, Q., Zhou, S., Louie, P.K.K., Luk, C.W.Y., 2015. Nitrous acid (HONO) in a polluted subtropical atmosphere: Seasonal variability, direct vehicle emissions and heterogeneous production at ground surface. Atmospheric Environment 106, 100-109.

Yu, H., Ren, L., Kanawade, V.P., 2017. New Particle Formation and Growth Mechanisms in Highly Polluted Environments. Current Pollution Reports 3, 10.1007/s40726-017-0067-3.

500 Yu, L., Wang, G., Zhang, R., Zhang, L., Song, Y., Wu, B., Li, X., An, K., Chu, J., 2013. Characterization and Source Apportionment of $PM_{2.5}$ in an Urban Environment in Beijing. Aerosol and Air Quality Research 13, 574-583.